

Charge Separation in a Niobate Nanosheet Photocatalyst Studied with Photochemical Labeling

Erwin M. Sabio,[†] Miaofang Chi,[‡] Nigel D. Browning,^{§,⊥} and Frank E. Osterloh^{*,†}

[†]Department of Chemistry, University of California, Davis, One Shields Avenue, Davis, California 95616,

[‡]Materials Science and Technology Division, Oak Ridge National Laboratory, Oak Ridge, Tennessee 37831,

[§]Department of Chemical Engineering and Materials Science, University of California, Davis, One Shields Avenue, Davis, California 95616, and [⊥]Lawrence Livermore National Laboratory, 7000 East Avenue, Livermore, California 94550

Received November 19, 2009. Revised Manuscript Received December 15, 2009

Photolabeling was employed to probe charge separation and the distribution of redox-active sites on the surface of nanosheets derived from the layered photocatalysts $\text{KCa}_2\text{Nb}_3\text{O}_{10}$. Electron microscopy reveals 1–50 nm particles of silver, gold, iridium oxide, and manganese dioxide particles and small atomically sized clusters of platinum and IrO_x on the nanosheet surfaces and along the edges. The sizes, shapes, and particle densities vary with the deposition conditions, i.e., the precursor concentration and the presence of sacrificial agents. Overall, the study shows that photogenerated electrons and holes are accessible throughout the nanosheets, without evidence for spatial charge separation across the sheet.

Introduction

Oxides of early transition metals (Ti, Nb, Ta) have evolved as effective photocatalysts for water splitting under UV irradiation—a process of potential importance for the conversion of abundant sunlight into renewable fuel.^{1–3} The efficiency of these catalysts is determined by several factors, including the visible light absorption characteristics of the material, the electrochemical overpotentials for the coupled water redox reactions, and the degree of photochemical charge separation. Measuring and understanding these separate processes are critical for raising the efficiency of photocatalysts.

One way to obtain information about charge separation in photocatalysts is by using *photochemical labeling*. During photochemical labeling, a catalyst powder is irradiated in the presence of a metal compound that deposits on the catalysts surface after a redox step. The locations of the deposited particles then pinpoint the redox-active sites. For TiO_2 anatase and rutile crystals, it was shown by Ohno et al. that photochemical deposition of PbO_2 (from Pb^{2+}) selectively occurs onto the (011) face, whereas platinum particles deposit reductively onto the (110) face.⁴ This indicates that the PbO_2 - and Pt-labeled crystals facets are the preferred locations for water oxidation and reduction, respectively. Similarly, photochemical labeling on La-doped NaTaO_3 showed that Pb^{2+} oxidatively deposits as PbO_2 in grooves on the catalyst surface, which were thus identified as sites for water oxidation.⁵ For microcrystals of the layered $\text{BaLa}_4\text{Ti}_4\text{O}_{15}$, deposition of PbO_2 identified the basal plane as water oxidation sites and the edge sites as water reduction sites (Au deposition).⁶ Finally,

photochemical deposition has also been employed on single crystalline titanate nanosheets. Here, Cu_2O , Au, and Cu were found to grow reductively on edge sites and MnO_2 to grow oxidatively on face sites of TiO_2 nanosheet.⁷ This was interpreted as evidence for electron hole separation occurring in the nanosheets, driving electrons to the edge sites and hole to the facets.

In this study, we apply photolabeling to evaluate charge separation and active site distribution in nanosheets derived from the Dion-Jacobsen phase $\text{KCa}_2\text{Nb}_3\text{O}_{10}$.^{8,9} $\text{KCa}_2\text{Nb}_3\text{O}_{10}$ is a well-known photocatalyst for H_2 evolution from water and from solutions of sacrificial electron donors.^{10–19} It has a layered structure that is composed of individual $\text{Ca}_2\text{Nb}_3\text{O}_{10}^-$ sheets (Figure 1), with each sheet made of layers of $\mu_2\text{-O}$ bridged NbO_6 octahedra and with Ca^{2+} ions filling the voids.

The layered structure type is believed to enhance catalytic activity because the reduced symmetry is thought to aid the separation of photochemically generated electrons and holes. For example, in the layered $\text{K}_2\text{La}_2\text{Ti}_3\text{O}_7$ it has been speculated

(7) Matsumoto, Y.; Ida, S.; Inoue, T. *J. Phys. Chem. C* **2008**, *112*(31), 11614–11616.

(8) Dion, M.; Ganne, M.; Tournoux, M. *Mater. Res. Bull.* **1981**, *16*(11), 1429–1435.

(9) Fukuoka, H.; Isami, T.; Yamanaka, S. *J. Solid State Chem.* **2000**, *151*(1), 40–45.

(10) Domen, K.; Yoshimura, J.; Sekine, T.; Tanaka, A.; Onishi, T. *Catal. Lett.* **1990**, *4*(4–6), 339–343.

(11) Ebina, Y.; Tanaka, A.; Kondo, J. N.; Domen, K. *Chem. Mater.* **1996**, *8*(10), 2534–2538.

(12) Takata, T.; Tanaka, A.; Hara, M.; Kondo, J. N.; Domen, K. *Catal. Today* **1998**, *44*(1–4), 17–26.

(13) Ebina, Y.; Sasaki, T.; Harada, M.; Watanabe, M. *Chem. Mater.* **2002**, *14*(10), 4390–4395.

(14) Kim, J.; Hwang, D. W.; Kim, H. G.; Bae, S. W.; Lee, J. S.; Li, W.; Oh, S. H. *Top. Catal.* **2005**, *35*(3–4), 295–303.

(15) Yamashita, Y.; Hyuga, K.; Petrykin, V.; Kakihana, M.; Yoshimura, M.; Domen, K.; Kudo, A. *J. Ceram. Soc. Jpn.* **2007**, *115*(1344), 511–513.

(16) Hata, H.; Kobayashi, Y.; Bojan, V.; Youngblood, W. J.; Mallouk, T. E. *Nano Lett.* **2008**, *8*(3), 794–799.

(17) Maeda, K.; Mallouk, T. E. *J. Mater. Chem.* **2009**, *19*(27), 4813–4818.

(18) Maeda, K.; Eguchi, M.; Youngblood, W. J.; Mallouk, T. E. *Chem. Mater.* **2009**, *21*(15), 3611–3617.

(19) Ebina, Y.; Sakai, N.; Sasaki, T. *J. Phys. Chem. B* **2005**, *109*(36), 17212–17216.

*Corresponding author: Fax (+1) 530 752 8995; Tel (+1) 530 752 6242; e-mail fosterloh@ucdavis.edu.

(1) Osterloh, F. E. *Chem. Mater.* **2008**, *20*(1), 35–54.

(2) Kudo, A.; Miseki, Y. *Chem. Soc. Rev.* **2009**, *38*(1), 253–278.

(3) Kamat, P. V. *J. Phys. Chem. C* **2007**, *111*(7), 2834–2860.

(4) Ohno, T.; Sarukawa, K.; Matsumura, M. *New J. Chem.* **2002**, *26*(9), 1167–1170.

(5) Kato, H.; Asakura, K.; Kudo, A. *J. Am. Chem. Soc.* **2003**, *125*(10), 3082–3089.

(6) Miseki, Y.; Kato, H.; Kudo, A. *Energy Environ. Sci.* **2009**, *2*(3), 306–314.

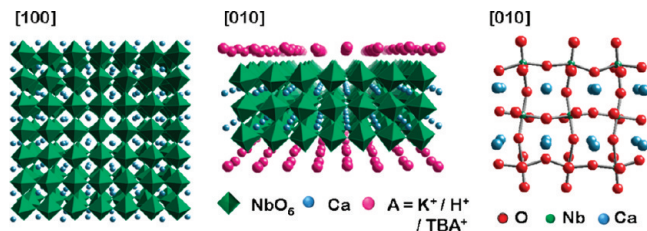


Figure 1. [TBA, H]- $\text{Ca}_2\text{Nb}_3\text{O}_{10}$ nanosheets consist of three layers of corner-sharing NbO_6 octahedra with Ca^{2+} ions in the voids. The surfaces and edges are terminated by $\mu_2\text{-O}^{2-}$ and terminal oxo ($\text{Nb}-\bar{\text{O}}$ and $\text{Nb}=\text{O}$) groups.

that holes oxidize water on interlayer sites, while electrons migrate to NiO cocatalyst particles deposited on edge sites.²⁰ For the NiO-intercalated $\text{K}_4\text{Nb}_6\text{O}_{17}$ phase, electrons and holes were suggested to migrate to different sites of the asymmetric nanosheets.²¹

We recently showed that when $\text{KCa}_2\text{Nb}_3\text{O}_{10}$ is chemically exfoliated into individual nanosheets,^{22–24} the photocatalytic activity of the niobate is retained, although in diminished form.^{25–28} Therefore, these nanosheets provide us with an opportunity to obtain further insight into the mechanism of photochemical charge separation on the nanoscale and to obtain information about the locations of the active sites on the catalyst surface.

Experimental Section

Reagents. K_2CO_3 , CaCO_3 , Nb_2O_5 , and $\text{TBA}(\text{OH})$ (40 wt % in H_2O) were purchased from Acros Organics, Morris Plains, NJ. $\text{H}_2\text{PtCl}_6 \cdot 6\text{H}_2\text{O}$, K_3IrCl_6 , $\text{MnSO}_4 \cdot \text{H}_2\text{O}$, and HNO_3 (70%) were purchased from Sigma-Aldrich, Milwaukee, WI. KNO_3 and AgNO_3 were obtained from Fisher Scientific, Pittsburgh, PA. Reagents were of reagent quality and used as received. Water used was purified to $> 18 \text{ M}\Omega \cdot \text{cm}$ resistivity using a Nanopure system.

Synthesis of Exfoliated Nanosheets. $\text{KCa}_2\text{Nb}_3\text{O}_{10}$ was synthesized from K_2CO_3 , CaCO_3 , and Nb_2O_5 using a published solid state synthesis procedure.^{24,29} $\text{HCa}_2\text{Nb}_3\text{O}_{10} \cdot 1.5\text{H}_2\text{O}$ was obtained following a 3-day proton exchange reaction of $\text{KCa}_2\text{Nb}_3\text{O}_{10}$ with 5 M HNO_3 .³⁰ Washed solid $\text{HCa}_2\text{Nb}_3\text{O}_{10}$ was stirred vigorously with 40% tetrabutylammonium hydroxide (TBA^+OH^-) for 5 days to form the exfoliated calcium niobate nanosheets (hereby designated as [TBA, H]- $\text{Ca}_2\text{Nb}_3\text{O}_{10}$).

Nanoparticle Loading onto Nanosheets. A colloidal suspension of [TBA, H]- $\text{Ca}_2\text{Nb}_3\text{O}_{10}$ was prepared by mixing 100 mg of nanosheets into 100 mL of water. Into this solution, 5.3 mg of $\text{H}_2\text{PtCl}_6 \cdot \text{H}_2\text{O}$, 3.5 mg of HAuCl_4 , 3.1 mg of AgNO_3 , 4.7 mg of K_3IrCl_6 , or 3.9 mg of MnSO_4 had been dissolved. These amounts corresponded to 2 wt % Pt, Au, Ag, IrO_x , and MnO_2 in reference

to the nanosheets. A second batch of the above solutions was prepared in 20% methanol for the Pt-, Au-, and Ag-containing reagents and in 5 mM KNO_3 for the IrO_x - and MnO_2 -containing reagents. A third batch was prepared for characterization purposes with 50 wt % loading of the photodeposition agents in pure water. The mixtures ($\text{pH} > 7$) were placed in a quartz flask and were degassed via three evacuation/Ar purge cycles. The mixtures were then stirred and irradiated for 1 h using a 300 W Cermex PE300BUV Xe lamp. Solid products were collected via centrifugation, washed twice with H_2O , and then stored in 15 mL of H_2O .

Instrumentation. Bright field transmission electron micrographs (BF-TEM) and dark field scanning TEM (DF-STEM) were collected using a JEOL 2500SE STEM with an accelerating voltage of 200 kV. STEM images were collected using ultrahigh-resolution ($< 0.5 \text{ nm}$) probe size at 500 mm camera length. Aberration-corrected high angle annular dark field STEM (HAADF-STEM) images were collected using an FEI Titan 300 kV microscope. Electron microscopy samples were mounted onto a 400-mesh Cu grid with lacey carbon film. UV/vis absorption spectra were collected using an Ocean Optics DH2000 light source and HR2000 CG UV-NIR spectrometer. For centrifugation, a Fisher Scientific Marathon 21000 centrifuge at 13 750 rpm was used.

Results

Before we present the photolabeling results, we briefly discuss the steps involved in the photochemical deposition of metal and metal oxides on the surface of [TBA, H]- $\text{Ca}_2\text{Nb}_3\text{O}_{10}$. The process (Figure 2) begins with (1) the generation of an electron–hole pair upon irradiation with UV light ($\lambda < 370 \text{ nm}$), which is followed by (2) charge trapping and (3) charge transfer to the metal complex or the sacrificial redox agent, leading to (4) nucleation and growth of the nanoparticles.

Measurements on TiO_2 have shown that excitons are generated on the femtosecond time scale.³¹ For [TBA,H]- $\text{Ca}_2\text{Nb}_3\text{O}_{10}$ nanosheets, transient absorption spectroscopy reveals that the formation of trapped electrons and holes (2) occurs about 200 fs after excitation, with the maximum of trapped charges formed about 1 ps after excitation.²⁷ Most charges recombine in the nanoseconds following excitation, but some of them are available for reaction with the surrounding water to produce hydrogen and peroxide.²⁵ When the sacrificial electron donor methanol is present, holes are quenched on the 0.1–1 ns time scale. The trapped electrons react more slowly (microseconds), as is known from studies for TiO_2 .³¹

To induce photochemical deposition, the metal precursors must first undergo a redox reaction with the nanosheets (step 3). The rate for this process is difficult to predict, as it will be affected by several parameters, including the redox potential of the metal complex, the number of transferred electrons, the concentration of metal complex in solution, and the electric charge of the metal complex (negatively charged precursors will be repulsed by the negatively charged nanosheets, whereas positively charged ones are attracted).

According to nucleation theory, the rates for nanoparticle nucleation and growth (step 4) will mainly depend on the unknown interfacial energies of the nanoparticle–nanosheet system. These energies will affect the critical nucleation radius (the smallest particle that can be nucleated) and thus determine the number density of particles that are growing on the sheets. After nucleation, the particle growth rate will likely be limited by the availability of charge carriers on the nanosheets (step 1) and by the kinetics of charge transfer (step 3).

(20) Takata, T.; Furumi, Y.; Shinohara, K.; Tanaka, A.; Hara, M.; Kondo, J. N.; Domen, K. *Chem. Mater.* **1997**, *9*(5), 1063–&.

(21) Domen, K. Water Photolysis by Layered Compounds. In *Photocatalysis Science and Technology*; Kaneko, M., Okura, I., Eds.; Springer: New York, 2002; pp 261–278.

(22) Treacy, M. M. J.; Rice, S. B.; Jacobson, A. J.; Lewandowski, J. T. *Chem. Mater.* **1990**, *2*(3), 279–286.

(23) Jacobson, A. J.; Lewandowski, J. T.; Johnson, J. W. *J. Less-Common Met.* **1986**, *116*(1), 137–146.

(24) Jacobson, A. J.; Johnson, J. W.; Lewandowski, J. T. *Inorg. Chem.* **1985**, *24*, 3727–3729.

(25) Compton, O. C.; Osterloh, F. E. *J. Phys. Chem. C* **2009**, *113*(1), 479–485.

(26) Compton, O. C.; Mullet, C. H.; Chiang, S.; Osterloh, F. E. *J. Phys. Chem. C* **2008**, *112*(15), 6202–6208.

(27) Carroll, E. C.; Compton, O. C.; Madsen, D.; Larsen, D. S.; Osterloh, F. E. *J. Phys. Chem. C* **2008**, *112*(7), 2394–2403.

(28) Compton, O. C.; Carroll, E. C.; Kim, J. Y.; Larsen, D. S.; Osterloh, F. E. *J. Phys. Chem. C* **2007**, *111*(40), 14589–14592.

(29) Dion, M.; Ganne, M.; Tournoux, M. *Mater. Res. Bull.* **1981**, *16*, 1429.

(30) Fang, M.; Kim, C. H.; Saupe, G. B.; Kim, H. N.; Waraksa, C. C.; Miwa, T.; Fujishima, A.; Mallouk, T. E. *Chem. Mater.* **1999**, *11*, 1526.

(31) Hoffmann, M. R.; Martin, S. T.; Choi, W. Y.; Bahnemann, D. W. *Chem. Rev.* **1995**, *95*(1), 69–96.

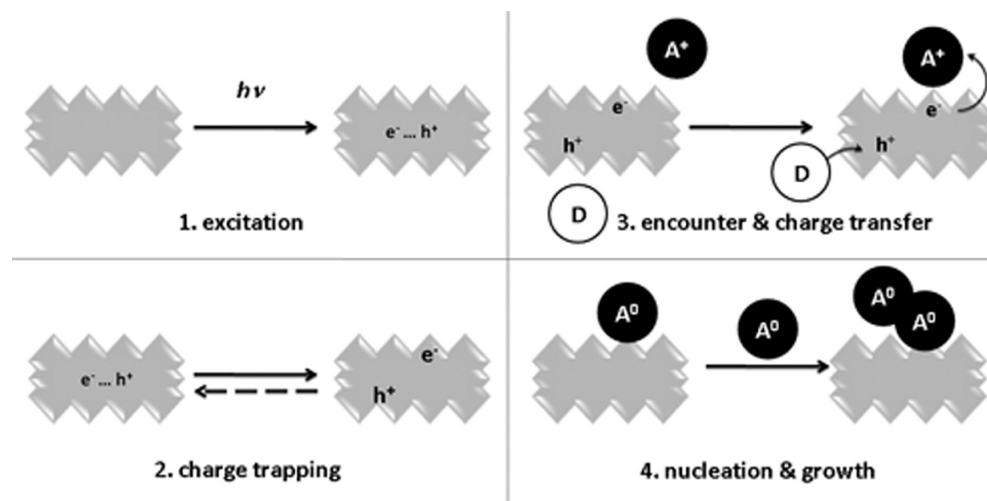


Figure 2. Steps involved in the photodeposition of metal and metal oxide particles on the [TBA,H]-Ca₂Nb₃O₁₀ nanosheets. D = Electron donor; A = Electron acceptor.

Table 1. Metal Precursors and Photogenerated Nanoparticles

reagent	product	no. of e ⁻ transferred	E ⁰ (V [NHE])	mean particle diameter (nm)			particle density (nm ⁻²)		
				2% in KNO ₃ or MeOH	2% in pure H ₂ O	50% in pure H ₂ O	2% in KNO ₃ or MeOH	2% in pure H ₂ O	50% in pure H ₂ O
AgNO ₃	Ag	+1	+0.8	0.97 ± 0.45	0.64 ± 0.16	7.6 ± 6.5	0.047 ± 0.006	0.050 ± 0.010	0.031 ± 0.007
H ₂ PtCl ₆	Pt	+4	+0.76	2.9 ± 0.9	0.82 ± 0.21	2.8 ± 1.1	0.040 ± 0.016	0.172 ± 0.031	0.019 ± 0.007
HAuCl ₄	Au	+3	+1.00	17 ± 9	1.1 ± 0.7	20 ± 11	0.00016 ± 0.000 20	0.00016 ± 0.000 13	0.00053 ± 0.000 01
K ₃ IrCl ₆	IrO _x	-1	-0.22	0.67 ± 0.76	0.40 ± 0.05	0.41 ± 0.19	0.089 ± 0.012	0.011 ± 0.008	0.041 ± 0.019
MnSO ₄	MnO ₂	-2	+1.22	11 ± 8	0.83 ± 0.16	51 ± 28	7.75 × 10 ⁻⁵ ± 1.46 × 10 ⁻⁵	0.075 ± 0.013	0.00013 ± 0.000 13

In principle, any of the steps in Figure 2 can limit the photo-deposition process and influence particle positions, particle size and shape, and the deposition rate. In order for photochemical deposition to have any diagnostic value with regard to the locations of trapped electrons and holes, experimental conditions must be chosen so that the rate of the overall deposition process is limited by the availability of trapped electrons and holes. To empirically approach these conditions, we have irradiated nanosheets in the presence of several photolabeling agents, varied their concentrations, and added/or withheld sacrificial agents. Of the reagents employed (see Table 1), H[AuCl₄], H₂[PtCl₆], and AgNO₃ are electron acceptors that are expected to deposit on electron trap sites on the nanosheets. On the other hand, MnSO₄ and K₃[IrCl₆] are expected to react with photogenerated holes to form MnO₂ and IrO_x, thus marking hole trap sites on the nanosheets.

For labeling, solutions of the respective metal complexes were mixed with dispersions of the nanosheets, and the resulting mixture was irradiated in an Ar atmosphere with a 300 W Xe arc lamp. The progress of photochemical deposition was followed optically. After 1 h of irradiation did the original color of the metal complexes disappear and colored solids of the photolabeled nanosheets were found to precipitate. Figure 3 shows dried films and diffuse reflectance visible spectra of the as-obtained products. Silver-loaded sheets appear deep red, and the spectrum shows broad absorption across the visible spectrum with relatively stronger intensities in the blue region. This broad absorption is expected for metallic silver, confirming reduction of silver(I). The Pt loaded nanosheets appear black, indicating that Pt(IV) in PtCl₆²⁻ was reduced to metallic Pt. The same occurs in the Au-loaded nanosheets, indicating the presence of finely divided Au.

The nanosheets irradiated with K₃IrCl₆ develop the characteristic blue color of colloidal IrO_x,³² which corresponds to a broad absorption centered at ~620 nm, indicative of Ir⁴⁺.³³

The locations, shape, crystallinity, and density of deposited nanoparticles were determined by TEM, SAED, HAADF-STEM, and HRTEM analysis. Selected data are summarized in Table 1.

Finally, the MnO₂-loaded sheets have the expected brown color of the Mn(IV) oxide that formed by oxidation of MnSO₄. This color is caused by a broad absorbance in the blue region that tapers to baseline at higher wavelengths. Overall, the visible spectra confirm the identities of the photodeposited materials as Ag, Au, Pt, IrO_x, and MnO₂.

Figure 4 shows electron micrographs for the Ag-deposited sheets. At 50 wt % loading in pure water (Figure 4A), quasi-spherical particles with a mean diameter of 7.6 ± 6.5 nm cover about ~23% of the sheet surface with a density of 0.050 nm⁻².

Figure 4B is a contrast-enhanced version of Figure 4A, highlighting regions with 1, 2, 3, and 4 nanosheets stacked upon each other. The image reveals an increase of the silver surface coverage with stack size. However, since the silver particle sizes are similar across the sample sections, we conclude that this change in coverage is due to nanosheet stacking after photochemical silver deposition and does not reflect different nanoparticle growth rates across the image regions. Figure 4C shows discrete crystalline particles that have lattice fringes oriented in two directions (green and orange lines). These sets of fringes appear as two pairs of identical reflections in the Fourier transform (FT) image (inset). The multiple orientations of the Ag crystals rule out epitaxial growth. At 2 wt % loading in the presence of the sacrificial electron donor methanol (Figure 4D), very small silver particles (0.97 ± 0.45 nm) start to dominate, which lack lattice

(32) Harriman, A.; Thomas, J. M.; Millward, G. R. *New J. Chem.* **1987**, *11*, 757.

(33) Nahor, C. S.; Hapiot, P.; Neta, P.; Harriman, A. J. *Phys. Chem.* **1991**, *95*, 616.

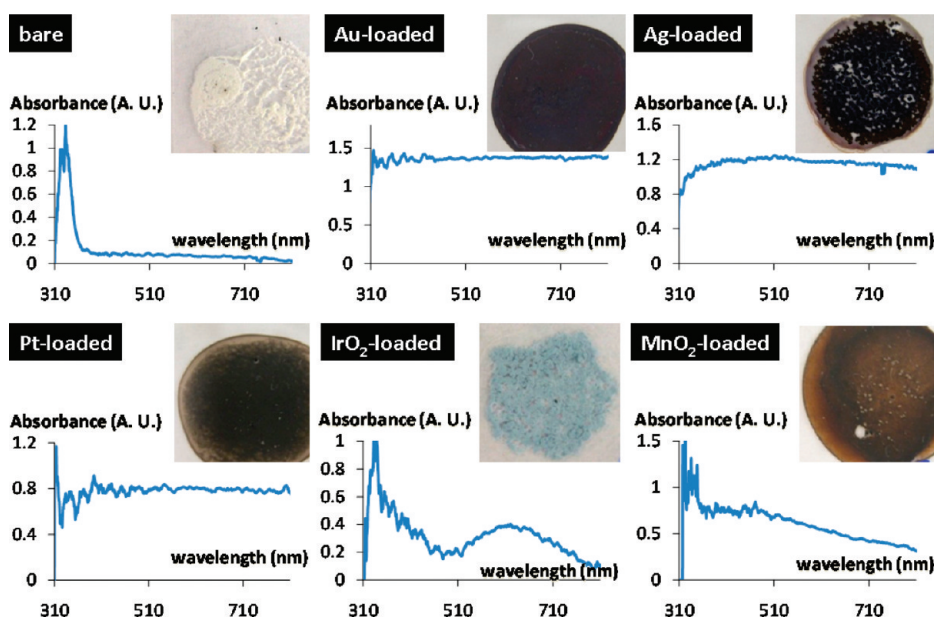


Figure 3. Diffuse reflectance spectra of the bare and photodeposited nanosheets. The samples were dried as thin films on glass slides (photos shown in inset).

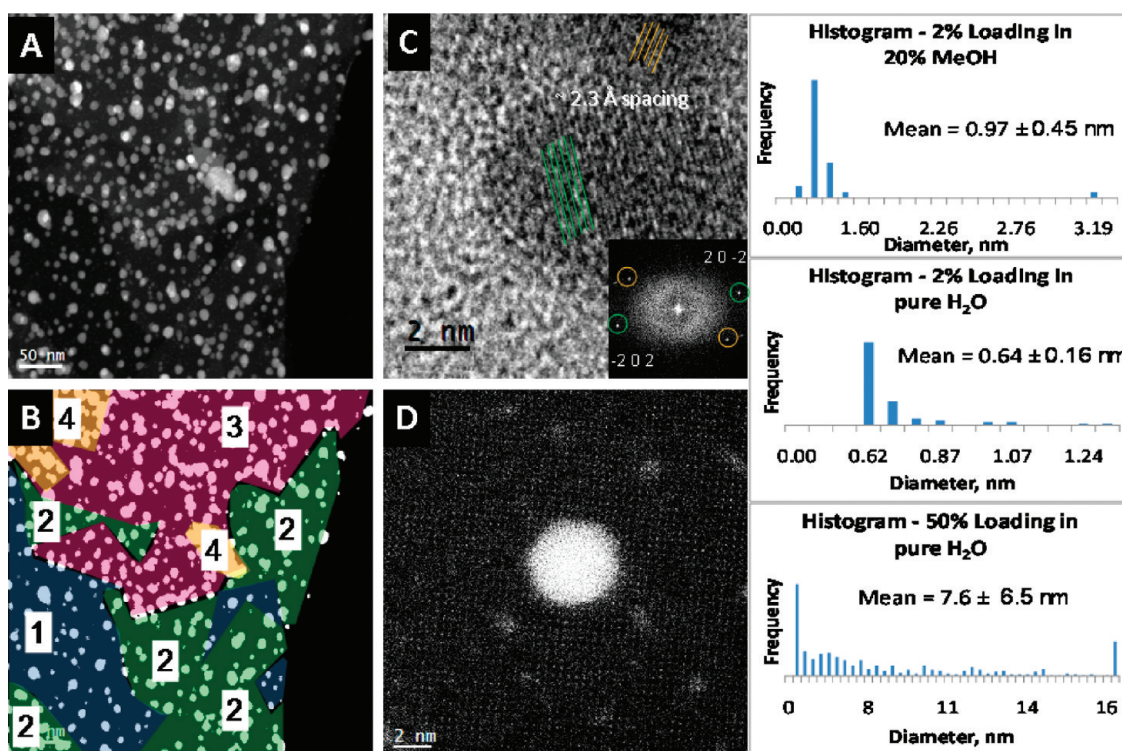


Figure 4. Electron micrographs and size distribution histograms of Ag-loaded [TBA, H]- $\text{Ca}_2\text{Nb}_3\text{O}_{10}$. (A) STEM image of sheets loaded with 50 wt % Ag in pure water and (B) color-enhanced version of the same image highlighting the increase of particle density with stacking (values indicate number of nanosheets). (C) HRTEM image of an Ag particle showing fringes corresponding to (202) and $(20\bar{2})$ reflections. (D) HAADF-STEM image of a typical Ag nanoparticle deposited in the presence of MeOH.

fringes and might be amorphous. With 0.017 nm^3 being the atomic volume for Ag, these nanoparticles are thought to consist of 5–90 Ag atoms. Because of the blurriness associated with these clusters, no exact atomic positions can be determined. The particles deposited in the absence of methanol ($\sim 0.64 \pm 0.16 \text{ nm}$) look similar (image not shown). While the net amount of deposited Ag at 2% is necessarily smaller than at 50%, the

particles densities (0.050 and 0.031 nm^{-2} in water) are about the same. This shows that Ag nucleation proceeds equally fast under the three conditions. No positional selectivity can be discerned. This suggests that photogenerated electrons are present throughout the nanosheet.

The morphology of photodeposited Pt is quite different from Ag. At 50 wt % deposition from pure water, Pt particles have a

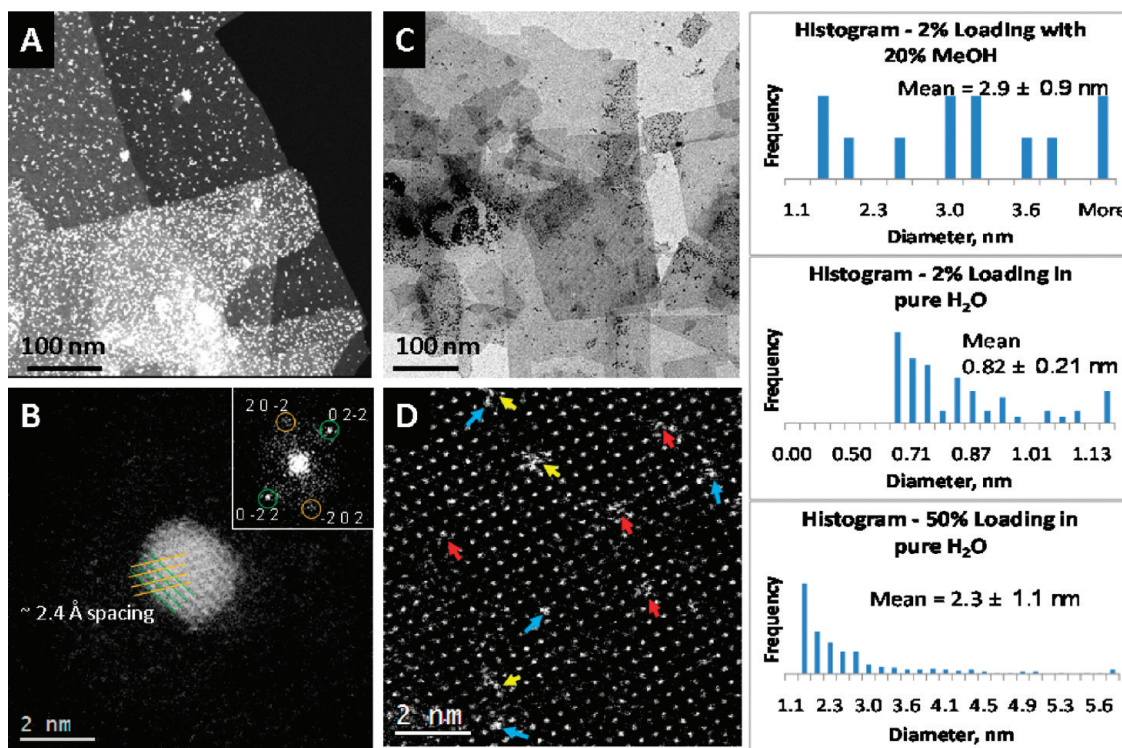


Figure 5. Electron micrographs and size distribution histograms of Pt-loaded [TBA, H]- $\text{Ca}_2\text{Nb}_3\text{O}_{10}$. (A) STEM image of sheets deposited with 50 wt % Pt in pure water. (B) HAADF-STEM image of a Pt particle oriented [111] with respect to the [100] sheet surface. (C) TEM image of sheets loaded with 2 wt % Pt in 20% MeOH. (D) HAADF-STEM image of a sheet with 2 wt % Pt loaded in pure water showing the positions of the Pt atoms with respect to the Nb columns of the sheet.

mean diameter of 2.3 ± 1.1 nm—about 3 times smaller than that of Ag. The TEM in Figure 5A shows Pt particles covering about 12% of a single nanosheet resulting in a particle density of 0.019 nm^{-2} . For the nanosheet stacks shown in the image, the density is 0.047 nm^{-2} for two sheets and 0.060 nm^{-2} for three sheets. That indicates that stacking occurred after the deposition. Many particles are agglomerated and, based on the lattice fringes, are polycrystalline with no epitaxial orientation with regard to the substrate. The particle shown in Figure 5B is oriented in the [111] direction while the underlying sheet is seen from the [100] direction. For the 2 wt % Pt deposited from aqueous methanol (Figure 5C), the particle size ($\sim 2.9 \pm 0.9$ nm) is similar to those deposited at 50 wt % in pure water. This time, particles appear arranged in large clusters, which indicates that they did not nucleate on the nanosheets but instead were adsorbed during sample preparation. In contrast, the 2 wt % Pt particles loaded in pure water are smaller ($\sim 0.82 \pm 0.21$ nm in diameter) and are found scattered throughout the sheet surface with particle density of 0.172 nm^{-2} . Using HAADF-STEM (D), it is possible to obtain atomic scale information about placement of the Pt atoms on the nanosheet. The nanosheet itself appears as a regular array of bright dots that correspond to the Nb atomic columns. Bridging these dots are μ_2 -oxygen atoms and in between are the Ca^{2+} ions (compare Figure 1). Because of their relatively lower mass compared to Nb, O and Ca are not visible in the z -contrast image. Platinum atoms are located either on top of Nb columns (blue arrows) or on top of μ_2 -O atoms (yellow arrows) or on top of Ca sites (red arrows). However, there is no apparent preference for either site.

The observed Au particles (Figure 6) are found to be larger than Pt and Ag for the same deposition conditions. When loaded at 50 wt % from pure water (Figure 6A), gold particles are crystalline (Figure 6B) and have an average diameter of 20 ± 11 nm. They cover 16% of the sheet surface with a very low

particle density of 0.0005 nm^{-2} . This shows that nucleation is the limiting factor for Au. When loaded in the presence of MeOH at 2 wt %, the Au particles prefer to cluster together in islands on sheet edges and between stacked sheets (Figure 6C). As discussed for Pt, this indicates that these particles nucleated in solution. In the absence of methanol, the 2 wt % loaded Au particles (Figure 6D) are smaller (mean diameter = 1.1 ± 0.7 nm) and the density is even lower (0.00016 nm^{-2}). For the first time, the particle distribution is not homogeneous. Instead, large particles are preferentially located on top of nanosheet stacks, while smaller particles are confined to single nanosheets. This indicates that the Au particles grew faster on nanosheet stacks than on single nanosheets. This supports the conclusion that nanosheet electrons were more accessible on the stacks, likely as a result of stronger light absorption. It also shows that electrons can migrate from one nanosheet to another to reach the Au growth sites.

IrO_x particles photodeposited via oxidation/hydrolysis of $\text{K}_3\text{-}[\text{IrCl}_6]$ are shown in the micrographs in Figure 7. The particles deposited at 50 wt % in pure water (Figure 7A) are very fine (0.41 ± 0.19 nm mean diameter) and amorphous. The particle density is comparatively small (0.041 nm^{-2}) with particles covering only 1.3% of the nanosheets. While many IrO_x nanoparticles are bonded to the nanosheet surface, a significant amount adsorbs to the nanosheet edges, suggesting that photogenerated holes are more accessible there. The edge-preferred deposition at higher precursor concentration could also reflect site-specific functionalization by the precursor ions, e.g., the entry of IrCl_6^{3-} into partial edge NbO_6 octahedra, just as observed in other layered compounds.³⁴ However, when the K_3IrCl_6 concentration is diminished, IrO_x preferentially deposits onto the nanosheet surfaces, even in the

(34) Kaschak, D. M.; Johnson, S. A.; Hooks, D. E.; Kim, H. N.; Ward, M. D.; Mallouk, T. E. *J. Am. Chem. Soc.* **1998**, *120*(42), 10887–10894.

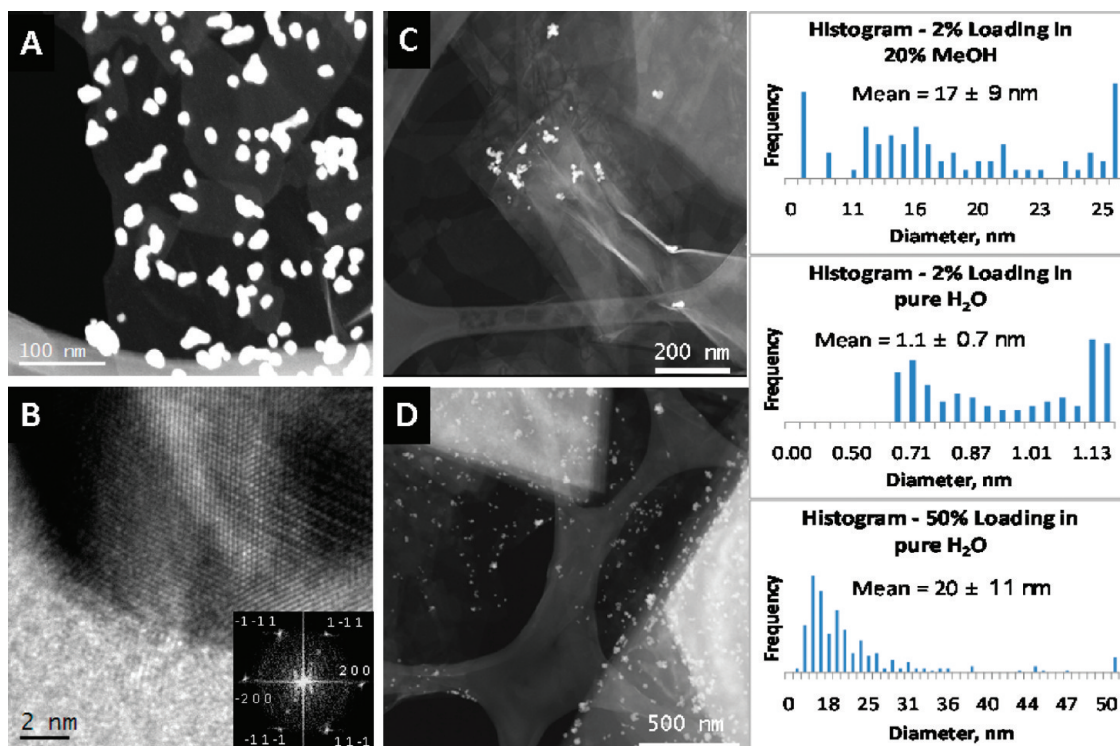


Figure 6. Electron micrographs and size distribution histograms of Au-loaded [TBA, H]-Ca₂Nb₃O₁₀. (A) STEM image of 50 wt % loaded sheets in pure water. (B) HRTEM image of a [111]-oriented Au particle on the [100] sheet surface. (C, D) STEM image of 2 wt % loaded sheets in 20% MeOH (C) and 2 wt % loaded sheets in pure water (D).

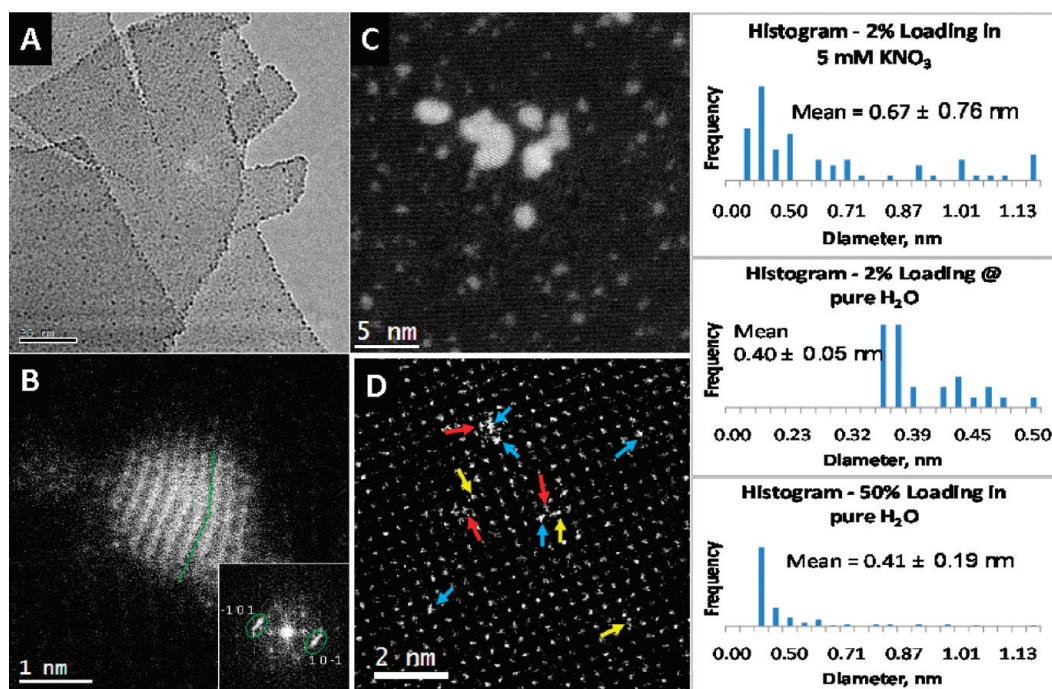


Figure 7. Electron micrographs and size distribution histograms of IrO_x-loaded [TBA, H]-Ca₂Nb₃O₁₀. (A) TEM image of 50 wt % loaded sheets in pure water. (B–D) HAADF-STEM images of an IrO_x particle (B), 2 wt % loaded sheets in KNO₃ solution (C), and 2 wt % loaded sheets in pure water (D).

presence of the sacrificial electron acceptor KNO₃ (Figure 7B). With KNO₃, the particles are slightly bigger (mean diameter 0.67 ± 0.76 nm) and the density is larger too (0.089 nm⁻²). Apparently, the IrO_x deposition is more complete in the presence of the electron acceptor. When deposited without KNO₃, the mean particle size

diminishes to 0.40 ± 0.05 nm and the particle density decreases (0.011 nm⁻²). In the HAADF-STEM image in Figure 7D, single cores or atoms of Ir can be distinguished on top of Nb sites (blue arrows), on top of Ca sites (red arrow), and on top of μ₂-O sites (yellow arrow), with no apparent preference for either site.

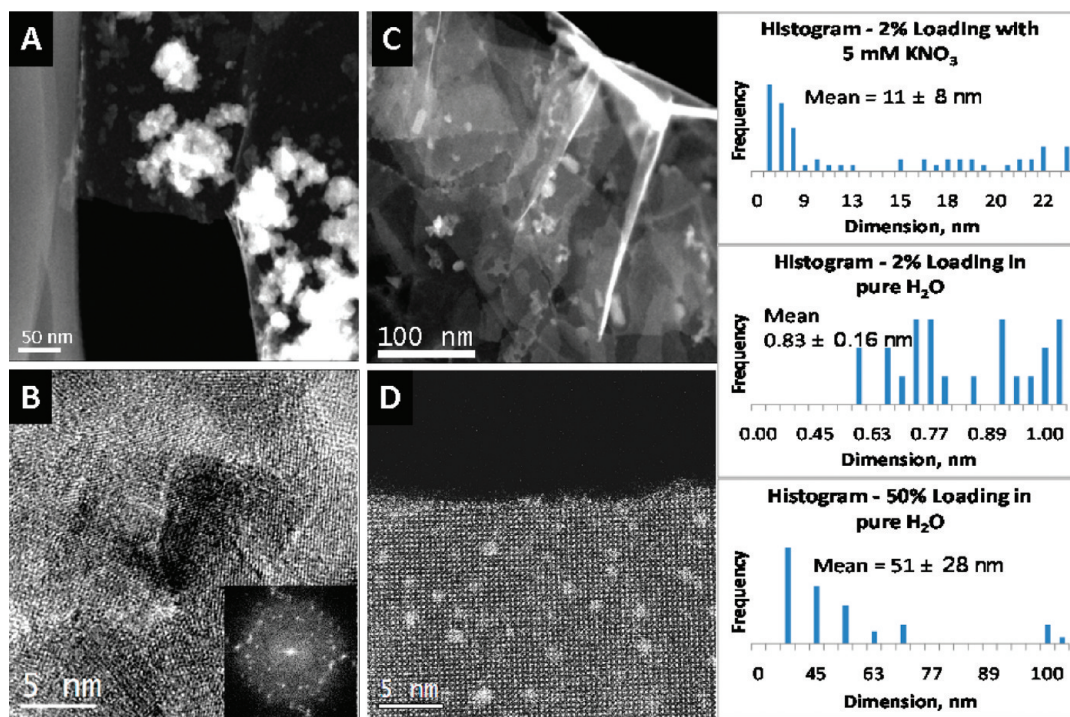


Figure 8. Electron micrographs and size distribution histograms of MnO₂-loaded [TBA, H]-Ca₂Nb₃O₁₀. (A) STEM image of sheets photodeposited with 50 wt % MnO₂ in pure water. (B) HRTEM image of overlapping MnO₂ nanocrystals. (C) STEM image of sheets loaded with 2 wt % MnO₂ in KNO₃ solution. (D) HAADF-STEM image of a 2 wt % MnO₂-loaded sheet in pure water.

To determine whether the nanosheet edge growth is due to photogenerated holes, MnSO₄ was used as an alternate hole-reactive reagent.

MnO₂ particles deposited at 50 wt % in water (Figure 8A) appear as irregular particles whose mean dimensions are difficult to define. Many particles reach lateral dimensions up to 150 nm, and are polycrystalline, based on the lattice fringes in Figure 8B (FT image in inset). At 2 wt % loading with KNO₃ as sacrificial electron acceptor (Figure 8C), the particles adopt a similar morphology, but they are smaller (mean width of only $\sim 11 \pm 8$ nm) and less aggregated. Without KNO₃ (Figure 8D), 2 wt % of MnO₂ deposit as small amorphous clusters of 0.83 ± 0.16 nm mean diameter and with a density of 0.075 nm^{-2} . In contrast to IrO_x, none of the MnO₂ crystals are found on the nanosheet edges, suggesting that photogenerated holes are accessible throughout the nanosheet.

Overall, the combined data (Table 1) show that nanoparticle sizes depend on the type of reagent used and on the experimental conditions of deposition. Specifically, we observe the following:

1. When sacrificial redox agents (MeOH or KNO₃) are present, the size of the particles is found to increase. That shows that sacrificial agents do raise the charge carrier concentrations in the nanosheets, thus promoting the rates of steps 3 and 4 (Figure 2) in the deposition. However, in the case of Pt and Au, sacrificial agents also lead to homogeneous nucleation and growth of nanoparticles. This may be a result of reactive byproducts (CH₂O, NO₂, radicals) formed upon partial reduction/oxidation of the sacrificial reagents, which can react with metal precursors in solution. Alternatively, homogeneous nucleation can result from disproportionation of partially reduced metal complexes. The fact that Ag does not nucleate homogeneously even in the presence of MeOH does support the latter interpretation.

2. With the exception of IrO_x, sacrificial agents do not increase the nanoparticle densities on the nanosheets. That suggests that

nucleation is not limited by the concentration of trapped charges, but by other factors, e.g. interfacial energies, and perhaps surface defects on the nanosheet surfaces. However, we were not able to observe such defects sites with the microscopy tools employed here.

3. Increasing the precursor concentration (from 2 to 50 wt %) has a strong effect on the average nanoparticle size. Since there is more precursor present, the net amount of photogenerated material can increase. With the exception of IrO_x, no increase in the nanoparticle densities is seen upon raising the concentration of the metal complexes. This supports the conclusion made under point 2, namely, that the heterogeneous nucleation rate is limited either by nanosheet surface defects or by nanoparticle interfacial energies.

4. Comparing particle sizes and densities across the series, the data shows that at 2% loading IrO_x and Ag particles are always the smallest, which suggests that nucleation is easier in these systems. This is likely due to the simple redox chemistry of these precursors, as only a single electron transfer step is required to give the products. Conversely, Au and Pt are much larger, likely as a result of the multistep electron transfers (3 and 4, respectively) involved in converting these metal complexes. The size of MnO₂ is difficult to compare with the other systems due to the flat morphology of these particles.

5. All reductive photolabels (Ag, Au, Pt) deposit only onto the nanosheet surfaces. This indicates that photogenerated electrons are accessible throughout the nanosheet surfaces. In the case of gold, the variable particle sizes found on single and stacked nanosheets show that growth is controlled by the availability of photogenerated electrons and that electrons can travel from nanosheet to nanosheet. For the hole-detecting labels (MnO₂, IrO_x) deposition occurs both on the nanosheet surfaces and on the nanosheet edges, in case of IrO_x (50% loading). That shows that, similar to the electrons, holes are evenly distributed on the nanosheets.

6. Photochemical deposition of Pt and Ir reagents produces near atomic size clusters on the nanosheets that can be directly observed with HAADF-STEM. Pt and Ir atoms were located randomly on top of μ_2 -bridging O sites, on top of Ca sites, and on top of Nb sites, with no apparent selectivity for either site.

Conclusion

In summary, we have used photolabeling to track the positions of redoxactive sites on the [TBA, H]-Ca₂Nb₃O₁₀ nanosheet water splitting photocatalyst. We find that size, number density, and crystallinity of the photodeposited nanoparticles depend on the nature of the labeling agents, their concentration, and the presence/absence of sacrificial agents. For all conditions, reductive and oxidative labels are found to deposit on nanosheet surface and edge sites. This means that photogenerated electrons and holes do not phase-separate on the nanosheets, contrary to what is observed for bulk semiconductors in contact with electrolytes. The main reason for the lack of separation is likely the small thickness of the nanosheets, which allows screening of any electric

(35) Kronik, L.; Ashkenasy, N.; Leibovitch, M.; Fefer, E.; Yoram, S.; Gorler, S.; Hodes, G. *J. Electrochem. Soc.* **1998**, *145*(5), 1748–1755.

(36) Gratzel, M. *Inorg. Chem.* **2005**, *44*(20), 6841–6851.

(37) Sodergren, S.; Hagfeldt, A.; Olsson, J.; Lindquist, S. E. *J. Phys. Chem.* **1994**, *98*(21), 5552–5556.

fields inside the sheet by the ions in solution. This prevents the formation of a space charge layer inside the niobate that could help pull electrons and holes apart. In the absence of an efficient mechanism for charge separation, the catalytic activity of the nanosheets must be attributed to preferential injection of either electrons or holes into the electrolyte, as is the case for other colloidal semiconductors³⁵ and for nanocrystal-based dye-sensitized cells.^{36,37} Thus charge generation and transfer of the nanosheet niobate appear to fundamentally differ from its layered parent phase. The beginning of electron–hole separation can be observed in the Au labeling experiments on [TBA, H]Ca₂Nb₃O₁₀ nanosheet stacks.

Lastly, we mention that our results on [TBA, H]-Ca₂Nb₃O₁₀ nanosheets disagree with earlier labeling studies on titanate nanosheets, where preferential growth of Cu₂O, Au, and Cu was observed on nanosheet edge sites.⁷ We believe that the observed edge deposition in that system is not due to electron–hole separation but must be attributed to other effects.

Acknowledgment. This work was supported by the National Science Foundation in the form of an “Energy for Sustainability” grant (CBET 0829142) and by the Department of Energy with Grant FG02-03ER46057. We also acknowledge support by the SHaRE User Facility at the Oak Ridge National Laboratory.